Cancer Immunology, Immunotherapy (2025) 74:113
https://doi.org/10.1007/s00262-025-03967-8

RESEARCH

Machine learning-derived prognostic signature integrating programmed cell death and mitochondrial function in renal clear cell carcinoma: identification of PIF1 as a novel target

Guangyang Cheng[1] · Zhaokai Zhou[1,2] · Shiqi Li[1] · Fu Peng[3] · Shuai Yang[1,2] · Chuanchuan Ren[1]

Received: 31 December 2024 / Accepted: 2 February 2025 / Published online: 25 February 2025

Abstract

Background The pathogenesis and progression of renal cell carcinoma (RCC) involve complex programmed cell death (PCD) processes. As the powerhouse of the cell, mitochondria can influence cell death mechanisms. However, the prognostic significance of the interplay between mitochondrial function (MF) and PCD remains unclear.

Methods We collected sets of genes related to PCD and MF. Using a powerful machine learning algorithm framework, we investigated the relationship between MF and PCD in different cohorts of patients and developed a machine learning-derived prognostic signature (mpMLDPS) related to MF and PCD. Finally, the most appropriate prognostic markers for RCC were screened by survival analysis and clinical correlation analysis, and the effects on renal cancer cells were analysed in vitro.

Results mpMLDPS was significantly correlated with the prognosis of RCC patients, and the prognosis was worse in the high mpMLDPS group, and this result was also validated in external independent cohorts. There were associations between mpMLDPS and immune checkpoints, tumour microenvironment, somatic mutations, and drug sensitivity. Finally, a novel RCC prognostic marker PIF1 was identified in model genes. The knockdown of PIF1 in vitro inhibited the progression of renal carcinoma cells.

Conclusion mpMLDPS has great potential to serve as a reliable clinical signature to improve the accuracy and reliability of prognostic assessment in RCC patients, thereby choosing the appropriate therapeutic regimen in clinical practice. PIF1 is also expected to be a novel target for the clinical treatment of RCC.

Keywords Mitochondria function · Programmed cell death · Kidney clear cell carcinoma · Machine learning · Prognostic signature · PIF1

Introduction

Renal cancer has a lower incidence rate than bladder cancer and prostate cancer among urological tumours, but it is the malignant tumour with the highest mortality rate in the urinary tract [1]. Clear cell renal cell carcinoma (ccRCC) is the most common and aggressive type of kidney cancer in adults. One-third of new RCC diagnoses have metastasised [2]. Patients with unresectable advanced RCC usually rely on immune checkpoint inhibitors (ICIs) or anti-angiogenic agents to prolong survival [3]. Additionally, the ICIs effect is often ineffective due to issues such as drug resistance, recurrence, and individual differences, improving the prognosis of renal cancer patients remains a major challenge [4]. Therefore, exploring novel therapeutic targets with consistent responsiveness is still necessary.

Guangyang Cheng, Zhaokai Zhou and Shiqi Li have contributed equally to this work.

✉ Chuanchuan Ren
cc_ren@zzu.edu.cn

[1] Department of Urology, The First Affiliated Hospital of Zhengzhou University, Zhengzhou 450052, Henan, China

[2] Bladder Structure and Function Reconstruction Henan Engineering Laboratory, The First Affiliated Hospital of Zhengzhou University, Zhengzhou 450052, Henan, China

[3] Department of Pharmacology, Key Laboratory of Drug-Targeting and Drug Delivery System of the Education Ministry, Sichuan Engineering Laboratory for Plant-Sourced Drug and Sichuan Research Center for Drug Precision Industrial Technology, West China School of Pharmacy, Sichuan University, Chengdu 610041, China

PCD is a controlled manner in which the body removes unwanted cells [5]. Mitochondria are double-membrane organelles in cells that regulate energy production, support cellular activities, and harbour metabolic pathways. Interestingly, it was found that mitochondria were not only a source of energy [6], but also determined cellular outcomes by regulating PCD [7]. However, the specific interactions between mitochondrial and PCD and their underlying mechanisms remain unclear. In clinical practice, TNM staging is a key determinant of prognosis in patients with tumours and is often used to understand the surgical approach and subsequent follow-up of patients [8]. Frustratingly, in numerous cases, tumours with nearly identical TNM staging and histologic types exhibit different prognostic differences and highly variable treatment responses [9]. Hence, it is essential to integrate novel biomarker data in a supplementary manner to offer insights that can enhance the prediction of outcomes.

Advances in next-generation sequencing technologies have led to a dramatic increase in research to identify biomarkers in tumours. A variety of genetic signatures for renal cancer prognosis have been established [10, 11]. However, these prognostic features are still deficient in terms of data utilisation, proper selection of modelling algorithms, and multi-cohort coverage [12]. Herein, we harnessed transcriptomic data to construct novel mpMLDPS related to PCD and MF. We also integrated machine learning algorithms to reduce the impact of various biases in sample selection on model accuracy and generalisability. Notably, we aimed to investigate the potential mechanisms by which PCD and MF influence prognosis and immunotherapy response. This may provide direction for tailored RCC treatment.

Methods

Transcriptome sequencing data acquisition

Transcriptome sequencing data and associated clinical information for the kidney renal clear cell carcinoma (KIRC) cohort from TCGA were downloaded from the GDC portal (https://portal.gdc.cancer.gov/). Gene microarray data and clinical information for the E-MTAB-1980 cohort and GSE167573 cohort were obtained from the ArrayExpress database (https://www.ebi.ac.uk/arrayexpress/) and gene expression omnibus (GEO) database (https://www.ncbi.nlm.nih.gov/geo/). The RNA-seq and microarray data were processed to remove genes with lower overall expression, and the expression values of the same genes were averaged. To make the gene expression values of different cohorts more comparable, we converted the gene expression values of different cohorts to a Z-Score and removed the patients with missing data of necessary clinical data. The set of PCD-related genes was collected [13, 14], and mitochondria-related genes were downloaded from the MitoCarta3.0 database (https://www.broadinstitute.org/) [15]. Detailed information is provided in Supplementary Table 1.

Construction of mpMLDPS

Differential expression analysis between tumour and normal tissues was performed on the Counts data of TCGA-KIRC using the "DESeq2" R package. Differentially expressed genes (DEGs) that met the criteria ($|\log2FC| > 1$ and adj.$p < 0.05$) were screened out. To obtain the intersection genes between DEGs and PCD, MF-related genes, the "VennDiagram" R package was used to take the intersection genes and generate Venn diagrams.

COX regression prognostic analyses were performed using intersecting genes, which were then screened for genes with $p < 0.05$ and the consistent hazard ratio (HR) trend in the three cohorts. We analysed the survival data by combining 10 different machine learning algorithms including resilient COX least squares regression (plsRcox), CoxBoost, elastic network regression (Enet), generalised boosted regression model (GBM), Lasso, Ridge, supervised principal component analysis (SuperPC), stepwise COX (Stepwise Cox), survival support vector machine (survival-SVM), and random survival forest (RSF). This combinatorial process resulted in a total of 76 unique algorithm combinations. The 76 algorithm combinations in the three cohorts were modelled using the identified prognostic genes. The C-index of each algorithm was calculated in different cohorts, and the algorithm combination with the highest average C-index was selected as the optimal model.

Immune microenvironment, immune checkpoint analysis, and immunotherapy response

The CIBERSORT algorithm was used to estimate the level of immune infiltration in the high and low mpMLDPS groups by analysing the enrichment of immune cells [16]. The differences in immune checkpoints between groups were further assessed. To predict immunotherapy response, we predicted the response of KIRC to ICIs using the tumour immune dysfunction and rejection (TIDE, http://tide.dfci.harvard.edu/login/) algorithm to determine the immunotherapy response rate in the high and low mpMLDPS groups.

Mutation mapping

To further explore the differences in genomic profiles between the high and low mpMLDPS groups, we defined the top 20 genes in terms of mutation frequency using the "maftool" R package. Subsequently, we calculated the tumour mutation rate (TMB) for each sample and performed survival analyses for the different subgroups.

Exploring potential therapeutic agents

To develop personalised therapeutic regimens for different risk categories, we comprehensively examined the gene expression and drug response information in the CCEL, CTRP and PRISM databases. Firstly, we calculated the mpMLDPS score of each cell line and categorised the cell lines into high and low mpMLDPS groups. Subsequently, we used analysis of variance to calculate the difference in AUC between compounds to determine the sensitive drug. A higher AUC indicates that the cell line is more sensitive to the drug. Subsequently, we compared the sensitivity of high and low AKT1 levels to sorafenib [17] to validate the accuracy of the method.

Clinical sample acquisition and immunohistochemistry (IHC)

The study was approved by the Ethics Committee of the First Affiliated Hospital of Zhengzhou University (2024-KY-0999-001), and all participants provided written informed consent. The study adhered strictly to the ethical principles outlined in the Declaration of Helsinki regarding medical research involving human subjects. Clinical samples were collected from patients diagnosed with RCC at the First Affiliated Hospital of Zhengzhou University. Paracancerous tissues were obtained from normal tissues located within 3 cm of the tumour. Tissue samples were immediately stored in liquid nitrogen and transferred to an ultra-low temperature freezer to preserve them for subsequent analysis.

Paraffin sections were deparaffinised and rehydrated, followed by heat-induced antigen retrieval using citrate nano-buffer solution. Endogenous peroxidase activity was blocked with 3% hydrogen peroxide solution, and non-specific binding was blocked with 3% BSA for 30 min at room temperature. The sections were incubated with the primary antibody overnight at 4 °C and with the secondary antibody for 50 min at room temperature. Target localisation was visualised using DAB staining, after which the sections were sealed and observed under a microscope.

Cell culture and cell transfection

Human kidney 2 cells (HK-2) and human renal cell adenocarcinoma lines (769-P, 786-O, and ACHN) were obtained from Servicebio (Wuhan, China). Renal carcinoma cell lines Caki-1, OS-RC-2, and A498 were purchased from Procell (Wuhan, China). HK-2, A498, and ACHN cells were cultured in MEM medium, while 769-P, OS-RC-2, and 786-O cells were maintained in RPMI-1640 medium. Caki-1 cells were cultured in McCoy's 5A medium. All media were supplemented with 10% foetal bovine serum (Cellbox, Changsha, China) and 1% penicillin–streptomycin. Cells were grown in a humidified incubator at 37 °C with 5% CO_2.

Cells were seeded in 6-well plates at a density of 10×10^4 cells per well to ensure a cell confluence of 20%–30% on the following day for transfection. The transfection system (medium + viral solution + transfection enhancer, total volume 1 mL; Genechem, Shanghai, China) was prepared and added on the next day. After 72 h of incubation, target gene expression was assessed by Western blot (WB). The medium was then replaced with complete medium containing puromycin to select for stably transfected strains. After 2–3 days of selection, the puromycin concentration was reduced to half of its initial working concentration to maintain culture. Meanwhile, cells were collected for verification by WB. Cells with confirmed identification results were cryopreserved for subsequent experiments.

WB analysis

Proteins from cells and tissues were extracted on ice using RIPA lysis buffer (containing 1% phosphatase inhibitor cocktail and PMSF). Protein concentration was determined using the BCA assay. The protein samples were then mixed with loading buffer, heated to achieve full denaturation, aliquoted, and stored at − 80 °C. Gels were prepared using the rapid gel preparation kit (Swiss Affinibody LifeScience AG, Wuhan, China) with the appropriate concentration, placed in the electrophoresis tank, the comb was removed, and samples were loaded. Electrophoresis was performed under constant voltage until completion. The PVDF membrane was activated with ethanol, placed in contact with the gel, and subjected to a constant flow of 400 mV for 30 min. Afterwards, the membrane was removed, washed, and blocked with 5% skimmed milk for 2 h. Subsequently, the membrane was incubated with primary antibody overnight at 4 °C, washed again the next day and then subjected to secondary antibody incubation at room temperature for 1 h. After washing, the membrane was imaged using an ECL luminescent solution. Primary antibodies used in this study: PIF1 (Proteintech, Wuhan, China), CDK2, CDK4, SOD2, P21 and Cleaved Caspase-9 (Zenbio, Chengdu, China).

Cell proliferation assay and clone formation experiment

For the cell proliferation assay, cells in the logarithmic growth phase were counted and seeded into 96-well plates at a density of 1000 cells per well. Separate 96-well plates were prepared for each time point, with five replicate wells set for each group. At the designated time points, 10 μL of CCK-8 solution (New Cell & Molecular Biotech, Guangzhou, China) was added to each well, followed by incubation in an incubator for 1 h. Absorbance values were then measured using a microplate reader.

For the colony formation assay, cells were digested with trypsin, counted, and seeded into 6-well plates at a density of 1000 cells per well. Cells were cultured in an incubator for 10 days, with the medium replaced every 3 days. Once visible colonies formed, the culture was terminated. Wells were washed three times with PBS, and cells were fixed with 4% paraformaldehyde for 30 min. After an additional PBS wash, 1 mL of crystal violet staining solution was added to each well to stain the cells for 20 min. The staining solution was then removed, and the wells were washed multiple times with PBS. The cells were air-dried and photographed.

Wound healing assay

Using a marker, three horizontal lines were drawn on the underside of a 6-well plate, spaced 0.5 cm apart. The cells to be tested were digested with trypsin, resuspended in medium, counted, and seeded into the 6-well plate at a density of 5×10^5 cells per well. Once the cells formed a confluent monolayer, a sterile 200 µL pipette tip was used to create vertical scratches across the horizontal lines on the bottom of the plate. After 24 h, the medium was aspirated, and the detached cells were removed by washing the wells three times with PBS. Cell migration was then observed under a microscope.

Transwell cell migration assay

The cells to be tested were digested with trypsin, resuspended in serum-free medium, and counted. A total of 20,000 cells in 200 µL of serum-free medium were seeded into the upper chamber of the Transwell insert, while the lower chamber was filled with 700 µL of complete medium containing 20% foetal bovine serum as a chemoattractant. After 24 h of incubation, the inserts were removed, and the non-migrated cells on the upper surface of the membrane were gently wiped off with a cotton swab. The migrated cells on the lower surface of the membrane were fixed with 4% paraformaldehyde for 20 min, washed with PBS, and stained with crystal violet solution. After staining, the membranes were washed with PBS, air-dried, and visualised under a microscope for image acquisition.

Reactive oxygen species (ROS) measurement

The cell culture medium was aspirated, and the cells were washed twice with PBS. DCFH-DA (TargetMol, Shanghai, China) was diluted to a final concentration of 10 µmol/L using serum-free medium. One millilitre of the diluted DCFH-DA solution was added to each well of a six-well plate, and the cells were incubated at 37 °C for 20 min in a cell culture incubator. After incubation, the cells were washed three times with serum-free medium to thoroughly remove any excess DCFH-DA that had not entered the cells. Fluorescent signals were observed and imaged using a fluorescence microscope.

Mitochondrial membrane potential

Cells were seeded in six-well plates and allowed to adhere. The culture medium was aspirated, and the cells were washed twice with PBS. One millilitre of TMRE staining working solution (0.5 µmol/L; TargetMol, Shanghai, China) was added to each well, along with 1 µL of Hoechst 33,342 solution (1 mg/mL), and the plate was incubated at 37 °C for 20 min in a cell culture incubator. After incubation, the supernatant was aspirated, and the cells were washed twice with pre-warmed culture medium. Two millilitres of pre-warmed culture medium were then added to each well. Fluorescent signals were observed and imaged using a fluorescence microscope.

Cell cycle analysis

A total of 1×10^6 cells were collected and centrifuged to remove the supernatant. The cells were washed twice with PBS and then fixed in 70% ethanol at 4 °C for 12 h. After fixation, the cells were centrifuged at 4 °C for 5 min, washed twice with PBS, and resuspended in 500 µL of PI staining solution. The mixture was thoroughly mixed and incubated at 37 °C for 30 min in the dark. Flow cytometry was then used to detect the cell cycle distribution, and the data were analysed using ModFit LT 5 software.

Statistics analysis

Data processing, analysis, and visualisation were performed using R software (version 4.3.2). Pearson correlation analysis was used to assess relationships between continuous variables. Comparisons of continuous variables were conducted using either the *t*-test or the Wilcoxon rank-sum test, depending on data distribution. Categorical variables were compared using Chi-square tests. Unless otherwise specified, statistical significance was defined as $p < 0.05$. Error bars represent 95% confidence intervals, and all statistical tests were two-tailed.

Results

Screening of PCD and MF-related prognostic genes and construction of mpMLDPS

The flow diagram is shown in Supplementary Fig. S1. Initially, we processed the TCGA-KIRC dataset and identified DEGs between tumour and normal tissues. A total of 6,150 DEGs were screened (Fig. 1b). We curated 1,575 regulatory genes associated with 19 PCD patterns and obtained 1,136 MF-related genes from the MitoCarta3.0 database. By intersecting these three datasets, we identified 192 MF-related DEGs and 429 PCD-related DEGs (Fig. 1c). To screen for genes involved in MF and PCD crosstalk, Pearson co-expression analysis was performed on the 192 differentially expressed MF-associated genes and 429 PCD-associated genes. 292 co-expressed genes were identified ($r > 0.6$ and $p < 0.001$). These 292 genes were subsequently analysed for prognosis in the TCGA-KIRC, E-MTAB-1980 and GSE167573 cohorts using COX regression. Finally, a total of 17 prognostically relevant genes with the same risk trend in all three cohorts ($p < 0.05$) were obtained (Fig. 1d). These 17 genes were subsequently utilised to develop the mpMLDPS using 76 combinations of machine learning algorithms. In the TCGA-KIRC training cohort, the performance of these combinations was evaluated through tenfold cross-validation, with the C-index serving as the metric for model robustness. To ensure generalisability, we calculated the average C-index across multiple validation cohorts (Fig. 1a). Among the tested models, Lasso + RSF achieved the highest average C-index (0.863). Coefficient path plots and cross-validation curves for the Lasso regression indicated that the optimal model contained eight genes, corresponding to the smallest λ value (Supplementary Fig. S2a, b). Additionally, we generated a bar chart ranking the importance of these eight genes in the RSF model (Supplementary Fig. S2c).

Performance evaluation of mpMLDPS

To evaluate the performance of mpMLDPS, we calculated the AUC and C-index in the three cohorts. The results demonstrated that the mpMLDPS model exhibited high accuracy, with 1/3/5-year AUC values of 0.900/0.952/0.803 in the GSE167573 cohort, 0.841/0.780/0.980 in the E-MTAB-1980 cohort, and 0.968/0.980/0.983 in the TCGA-KIRC cohort (Fig. 2a). As illustrated in Fig. 2b, the mpMLDPS achieved a C-index value (95% confidence interval) of 0.863 (0.827–0.899) in the GSE167573 cohort, 0.784 (0.732–0.836) in the E-MTAB-1980 cohort, and 0.943 (0.938–0.948) in the TCGA-KIRC cohort. Patients were stratified into high and low mpMLDPS groups based on the median cutoff value. Kaplan–Meier survival analysis revealed that patients in the high mpMLDPS group had a significantly worse prognosis, with shorter overall survival (OS) compared to the low mpMLDPS group across all cohorts (Fig. 2c–e).

Nomogram construction

To facilitate the clinical application of mpMLDPS, we constructed a nomogram. Initially, univariate and multivariate survival analyses were conducted for age, gender, tissue grade, clinical stage, and mpMLDPS (Fig. 3a, b). Among these factors, age ($p < 0.001$, HR = 1.025, 95% CI = 1.012–1.038) and mpMLDPS ($p < 0.001$, HR = 1.048, 95% CI = 1.042–1.053) were identified as significant in both analyses. Subsequently, these two independent prognostic factors were incorporated into a clinically applicable nomogram (Fig. 3c). Both calibration curves and ROC curves indicated that the nomogram demonstrated excellent accuracy and stability. Furthermore, we calculated the AUC values for mpMLDPS and commonly used clinical metrics. The results showed that the AUC of mpMLDPS was 0.984, compared to 0.722 for Clinical Stage and 0.680 for Pathology Grade, underscoring the superior generalizability and performance of mpMLDPS relative to traditional clinical features (Fig. 3d, e).

Immune microenvironment analysis and immunotherapeutic response

To further explore the differences in the expression of immune checkpoints in the mpMLDPS subgroups, we selected representative immune checkpoints for analysis and screened out the $p < 0.05$ immune checkpoints to draw a box plot (Fig. 4a). Specifically, CD28, CTLA4, PDCD1, and TIGIT in the high mpMLDPS group expressed at higher levels ($p < 0.05$). In contrast, NRP1, CD274, and CD200 were expressed higher in the low mpMLDPS group. Meanwhile, we calculated the percentage of immune cell infiltration in all TCGA-KIRC samples by the CIBERSORT algorithm (Fig. 4b). The results showed that the infiltration proportions of activated-state CD4 T cells memory, regulatory T cells (Tregs) and follicular helper T cells were significantly higher in the high mpMLDPS group than in the low mpMLDPS group ($p < 0.05$). Subsequently, StromalScore, ImmuneScore, TumorPurity, and ESTIMATEScore using the ESTIMATE algorithm were calculated (Fig. 4c, d, f, g), and the StromalScore, ImmuneScore, and ESTIMATEScore of the high mpMLDPS group were all significantly higher than the low MLDPS group ($p < 0.01$). Additionally, tumour purity analysis showed that the high mpMLDPS group had lower tumour purity ($p < 0.0001$), which was consistent with its

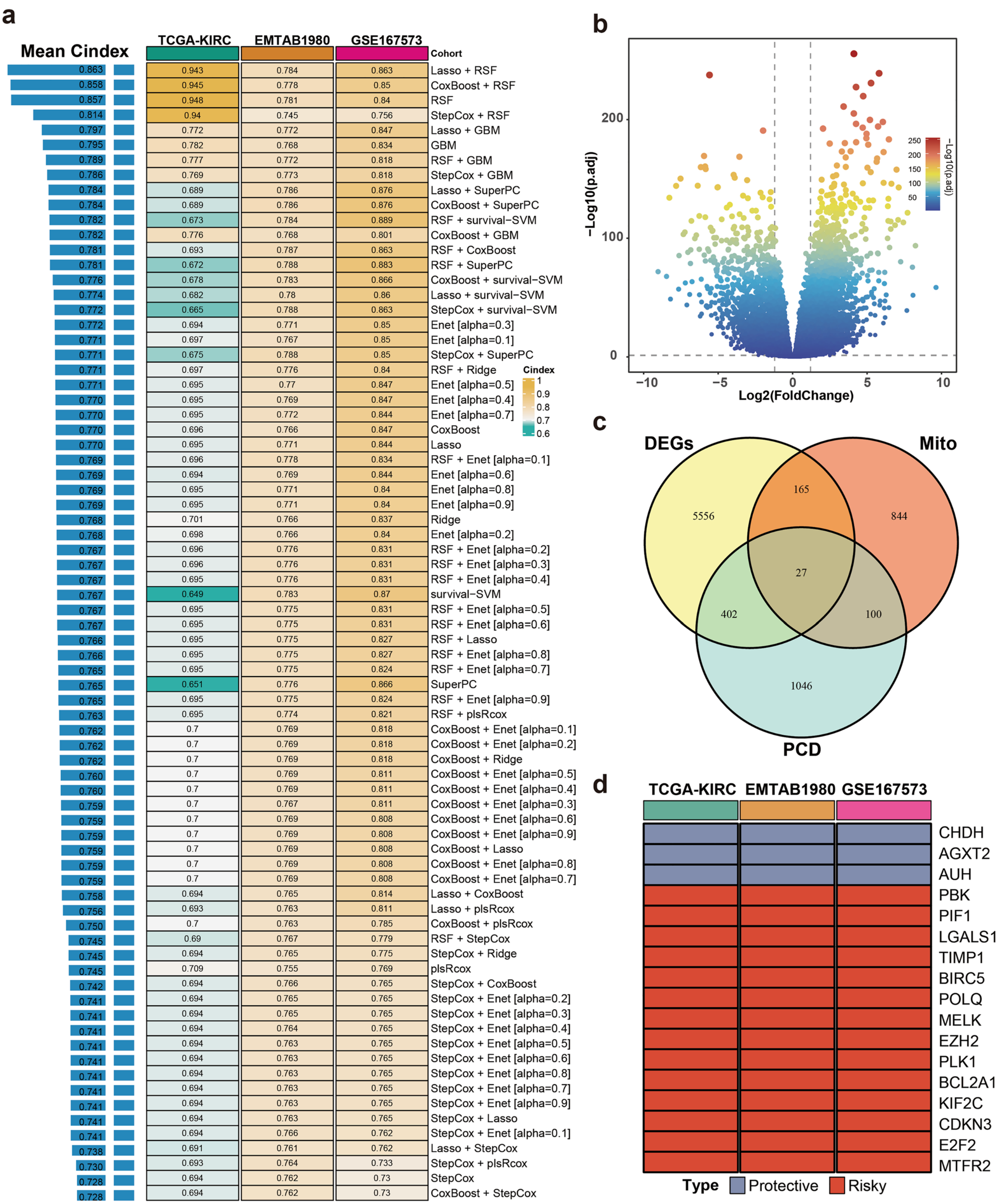

Mean Cindex	TCGA-KIRC	EMTAB1980	GSE167573	
0.863	0.943	0.784	0.863	Lasso + RSF
0.858	0.945	0.778	0.85	CoxBoost + RSF
0.857	0.948	0.781	0.84	RSF
0.814	0.94	0.745	0.756	StepCox + RSF
0.797	0.772	0.772	0.847	Lasso + GBM
0.795	0.782	0.768	0.834	GBM
0.789	0.777	0.772	0.818	RSF + GBM
0.786	0.769	0.773	0.818	StepCox + GBM
0.784	0.689	0.786	0.876	Lasso + SuperPC
0.784	0.689	0.786	0.876	CoxBoost + SuperPC
0.782	0.673	0.784	0.889	RSF + survival−SVM
0.782	0.776	0.768	0.801	CoxBoost + GBM
0.781	0.693	0.787	0.863	RSF + CoxBoost
0.781	0.672	0.788	0.883	RSF + SuperPC
0.776	0.678	0.783	0.866	CoxBoost + survival−SVM
0.774	0.682	0.78	0.86	Lasso + survival−SVM
0.772	0.665	0.788	0.863	StepCox + survival−SVM
0.772	0.694	0.771	0.85	Enet [alpha=0.3]
0.771	0.697	0.767	0.85	Enet [alpha=0.1]
0.771	0.675	0.788	0.85	StepCox + SuperPC
0.771	0.697	0.776	0.84	RSF + Ridge
0.771	0.695	0.77	0.847	Enet [alpha=0.5]
0.770	0.695	0.769	0.847	Enet [alpha=0.4]
0.770	0.695	0.772	0.844	Enet [alpha=0.7]
0.770	0.696	0.766	0.847	CoxBoost
0.770	0.695	0.771	0.844	Lasso
0.769	0.696	0.778	0.834	RSF + Enet [alpha=0.1]
0.769	0.694	0.769	0.844	Enet [alpha=0.6]
0.769	0.695	0.771	0.84	Enet [alpha=0.8]
0.769	0.695	0.771	0.84	Enet [alpha=0.9]
0.768	0.701	0.766	0.837	Ridge
0.768	0.698	0.766	0.84	Enet [alpha=0.2]
0.767	0.696	0.776	0.831	RSF + Enet [alpha=0.2]
0.767	0.696	0.776	0.831	RSF + Enet [alpha=0.3]
0.767	0.695	0.776	0.831	RSF + Enet [alpha=0.4]
0.767	0.649	0.783	0.87	survival−SVM
0.767	0.695	0.775	0.831	RSF + Enet [alpha=0.5]
0.767	0.695	0.775	0.831	RSF + Enet [alpha=0.6]
0.766	0.695	0.775	0.827	RSF + Lasso
0.766	0.695	0.775	0.827	RSF + Enet [alpha=0.8]
0.765	0.695	0.775	0.824	RSF + Enet [alpha=0.7]
0.765	0.651	0.776	0.866	SuperPC
0.765	0.695	0.775	0.824	RSF + Enet [alpha=0.9]
0.763	0.695	0.774	0.821	RSF + plsRcox
0.762	0.7	0.769	0.818	CoxBoost + Enet [alpha=0.1]
0.762	0.7	0.769	0.818	CoxBoost + Enet [alpha=0.2]
0.762	0.7	0.769	0.818	CoxBoost + Ridge
0.760	0.7	0.769	0.811	CoxBoost + Enet [alpha=0.5]
0.760	0.7	0.769	0.811	CoxBoost + Enet [alpha=0.4]
0.759	0.7	0.767	0.811	CoxBoost + Enet [alpha=0.3]
0.759	0.7	0.769	0.808	CoxBoost + Enet [alpha=0.6]
0.759	0.7	0.769	0.808	CoxBoost + Enet [alpha=0.9]
0.759	0.7	0.769	0.808	CoxBoost + Lasso
0.759	0.7	0.769	0.808	CoxBoost + Enet [alpha=0.8]
0.759	0.7	0.769	0.808	CoxBoost + Enet [alpha=0.7]
0.758	0.694	0.765	0.814	Lasso + CoxBoost
0.756	0.693	0.763	0.811	Lasso + plsRcox
0.750	0.7	0.763	0.785	CoxBoost + plsRcox
0.745	0.69	0.767	0.779	RSF + StepCox
0.745	0.694	0.765	0.775	StepCox + Ridge
0.745	0.709	0.755	0.769	plsRcox
0.742	0.694	0.766	0.765	StepCox + CoxBoost
0.741	0.694	0.765	0.765	StepCox + Enet [alpha=0.2]
0.741	0.694	0.765	0.765	StepCox + Enet [alpha=0.3]
0.741	0.694	0.764	0.765	StepCox + Enet [alpha=0.4]
0.741	0.694	0.763	0.765	StepCox + Enet [alpha=0.5]
0.741	0.694	0.763	0.765	StepCox + Enet [alpha=0.6]
0.741	0.694	0.763	0.765	StepCox + Enet [alpha=0.8]
0.741	0.694	0.763	0.765	StepCox + Enet [alpha=0.7]
0.741	0.694	0.763	0.765	StepCox + Enet [alpha=0.9]
0.741	0.694	0.763	0.765	StepCox + Lasso
0.741	0.694	0.766	0.762	StepCox + Enet [alpha=0.1]
0.738	0.691	0.761	0.762	Lasso + StepCox
0.730	0.693	0.764	0.733	StepCox + plsRcox
0.728	0.694	0.762	0.73	StepCox
0.728	0.694	0.762	0.73	CoxBoost + StepCox

TCGA-KIRC	EMTAB1980	GSE167573	
🟦	🟦	🟦	CHDH
🟦	🟦	🟦	AGXT2
🟦	🟦	🟦	AUH
🟥	🟥	🟥	PBK
🟥	🟥	🟥	PIF1
🟥	🟥	🟥	LGALS1
🟥	🟥	🟥	TIMP1
🟥	🟥	🟥	BIRC5
🟥	🟥	🟥	POLQ
🟥	🟥	🟥	MELK
🟥	🟥	🟥	EZH2
🟥	🟥	🟥	PLK1
🟥	🟥	🟥	BCL2A1
🟥	🟥	🟥	KIF2C
🟥	🟥	🟥	CDKN3
🟥	🟥	🟥	E2F2
🟥	🟥	🟥	MTFR2

Type 🟦 Protective 🟥 Risky

Fig. 1 Screening of PCD and MF-related differential genes and construction of mpMLDPS. **a** C-index values of 76 combinations of machine learning algorithms valuated across different cohorts. **b** Volcano plot of differentially expressed genes between tumour and paracancerous tissues in the TCGA-KIRC dataset. **c** Venn diagram showing the intersection of differentially expressed genes, PCD-related genes, and MF-related genes. **d** Genes with the same risk trend in the profiles of the three cohorts

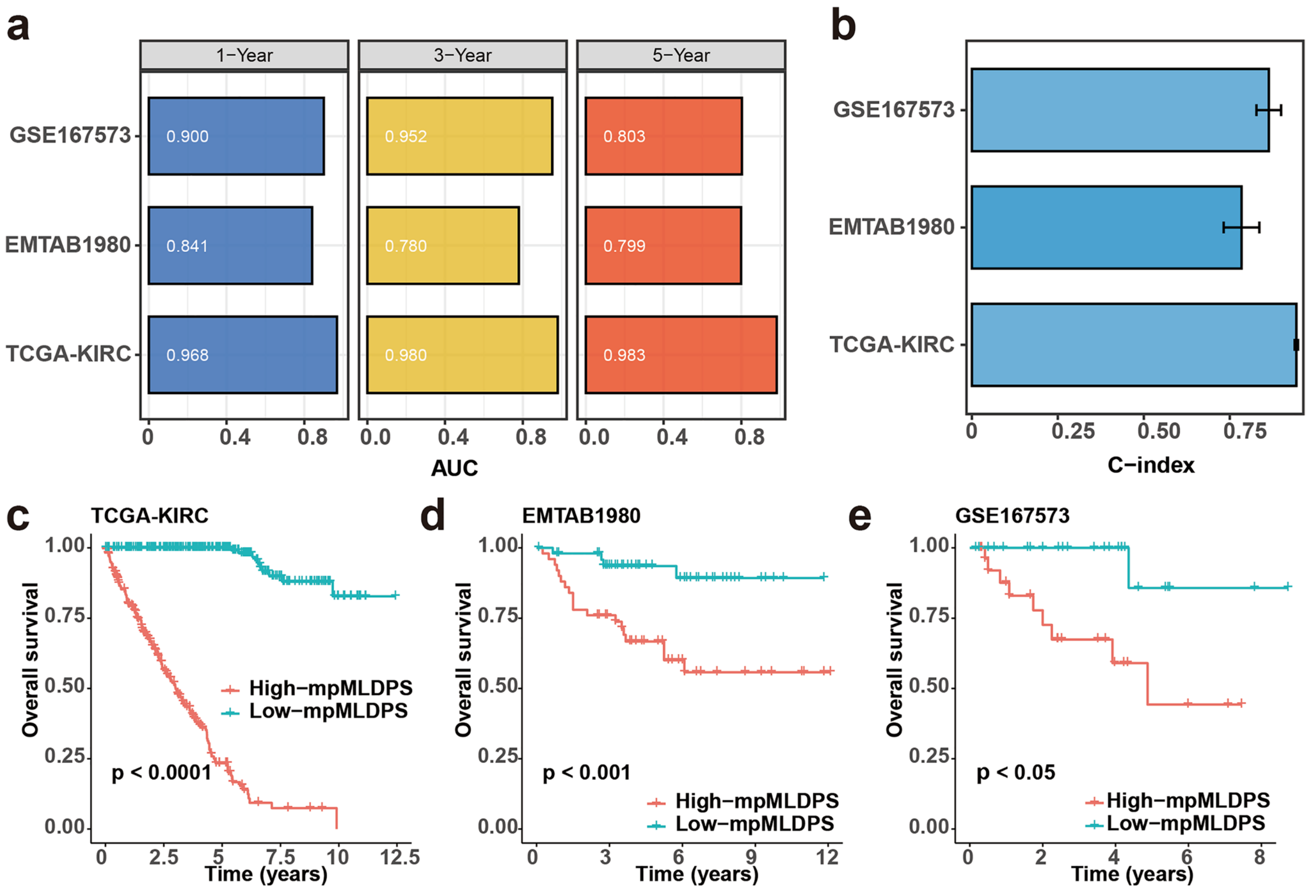

Fig. 2 Predictive performance of mpMLDPS in kidney cancer cohorts. **a** AUC values of mpMLDPS for 1-, 3- and 5-year OS prediction in three cohorts (GSE167573, EMTAB1980, and TCGA-KIRC). **b** C-index for the three cohorts, error bars represent 95% confidence intervals. **c-e** Kaplan–Meier survival curves for OS in the high and low mpMLDPS groups in the TCGA-KIRC, E-MTAB-1980, and GSE167573 cohorts

rich stroma and immune cell infiltration. Finally, to assess the difference in response to immunotherapy between the two groups, TIDE analysis showed that the TIDE score was significantly higher in the high mpMLDPS group than in the low mpMLDPS group ($p < 0.01$, Fig. 4h). The immunotherapy response rate analysis also showed that the response rate of the low mpMLDPS group (43%) was significantly higher than the high mpMLDPS group (34%), which further validated the predictive performance of the TIDE score for immunotherapy response ($p = 0.03219$, Fig. 4e).

Exploring somatic mutation differences between two subgroups and identifying potential drugs effective for high mpMLDPS group

Waterfall plot analysis was conducted using CNV data from the TCGA-KIRC cohort (Fig. 5a, b), showcasing the top 20 high-frequency mutated genes in both high and low mpMLDPS groups via the "maftools" R package. Stratifying patients by median TMB revealed that those in the high TMB group had a worse prognosis compared to the low TMB group (Fig. 5c). Joint survival analysis of TMB and mpMLDPS subgroups demonstrated the worst prognosis in patients with both high TMB and high mpMLDPS (Fig. 5d). Additionally, TMB was significantly elevated in the high mpMLDPS group compared to the low mpMLDPS group (Fig. 5e).

To investigate differences in drug sensitivity between subgroups, gene expression and drug sensitivity data from cell lines were systematically collected from the CTRP and PRISM databases. The accuracy of this approach was validated before identifying subgroup-specific sensitive drugs. Consistent with previous studies, reduced AKT1 levels have been shown to enhance RCC sensitivity to sorafenib, a targeted therapeutic drug [17]. Using CCLE, PRISM, and CTRP databases, drug sensitivity predictions yielded highly accurate results (Fig. 5g). A total of 12 candidate drugs potentially effective for high mpMLDPS patients were identified, including 5 drugs from CTRP (3-CI-AHPC, CD-437, pevonedistat, STF-31, and leptomycin B) and 7

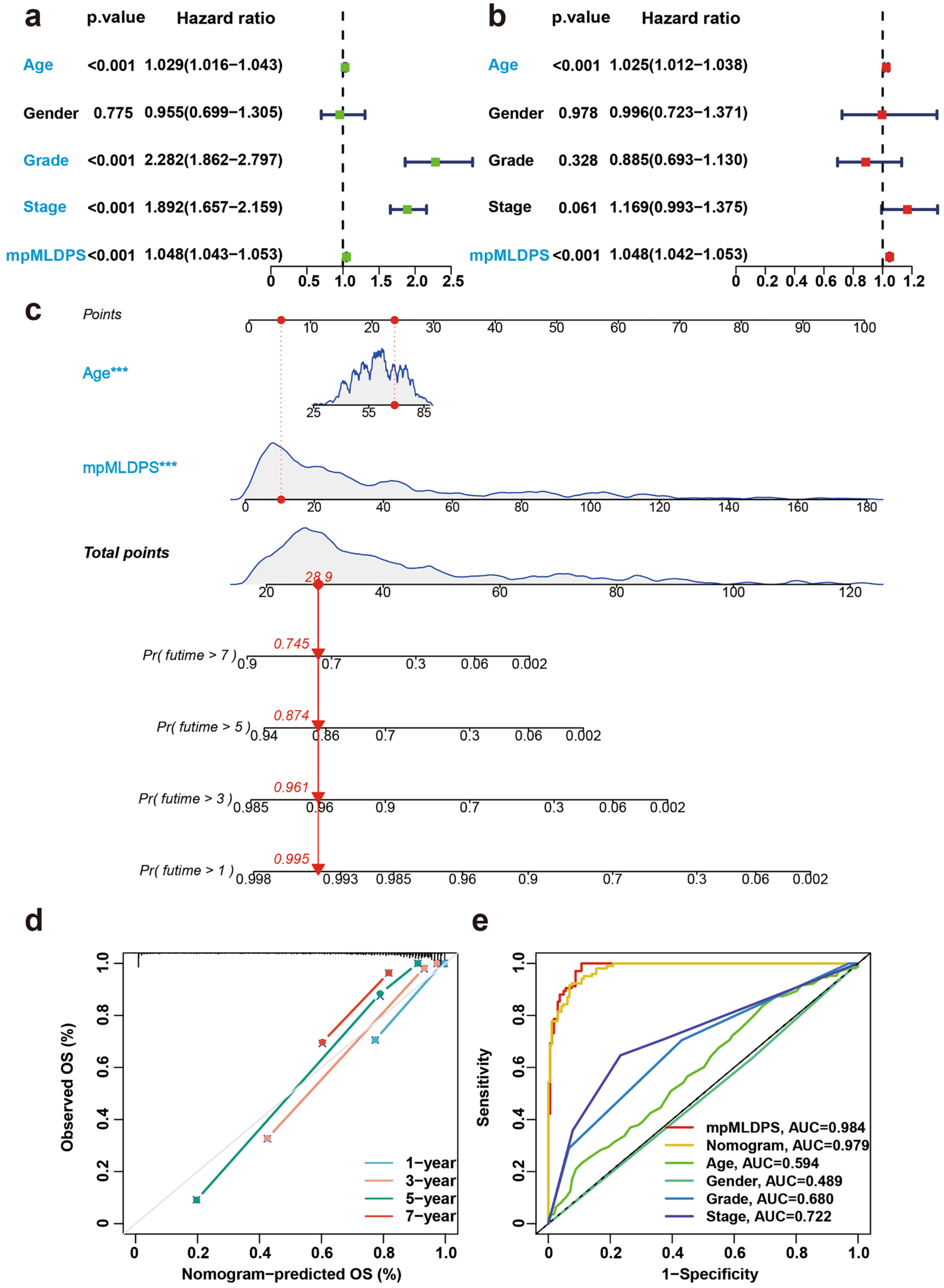

Fig. 3 Construction and calibration of nomogram for clinical practice. **a–b** Univariate and multivariate survival analysis of prognostic factors. **c** Normogram for clinical use. **d–e** Calibration curves and ROC curves for nomogram

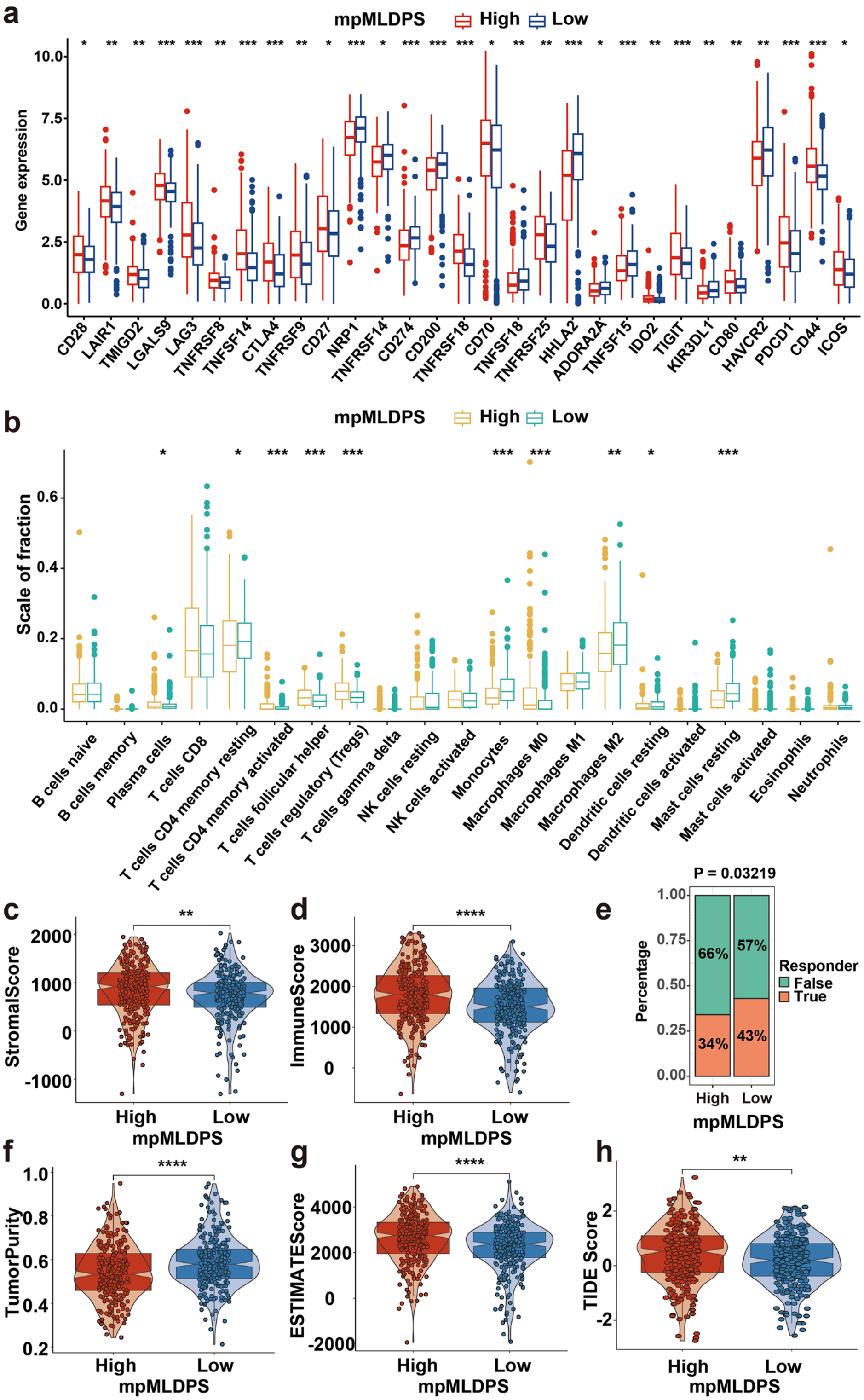

Fig. 4 Differences in the immune microenvironment and differences in immunotherapeutic response in mpMLDPS subgroups. **a**–**b** Box line plots of differences in immune cell infiltration and differences in immune checkpoint expression in mpMLDPS subgroups. **c**–**d** Box line plot of StromalScore and ImmuneScore differences in mpMLDPS subgroups. **e** Differences in the proportion of immunotherapy responses in mpMLDPS subgroups. **f**–**g** Box line plot of TumorPurity and ESTNIATEScore differences in mpMLDPS subgroups. **h** Box line plot of TIDEScore differences in mpMLDPS subgroups. $*p < 0.05$; $**p < 0.01$; $***p < 0.001$; $****p < 0.0001$

drugs from PRISM (MK-2461, harringtonine, paliperidone, gemcitabine, VE-822, daunorubicin, and BF2.649) (Fig. 5f).

Differential expression of model genes, survival and enrichment analysis

In this study, the final modelling genes for the LASSO + RSF model were identified as PIF1, TIMP1, PLK1, E2F2, BCL2A1, CHDH, AGXT2, and AUH. To explore their roles

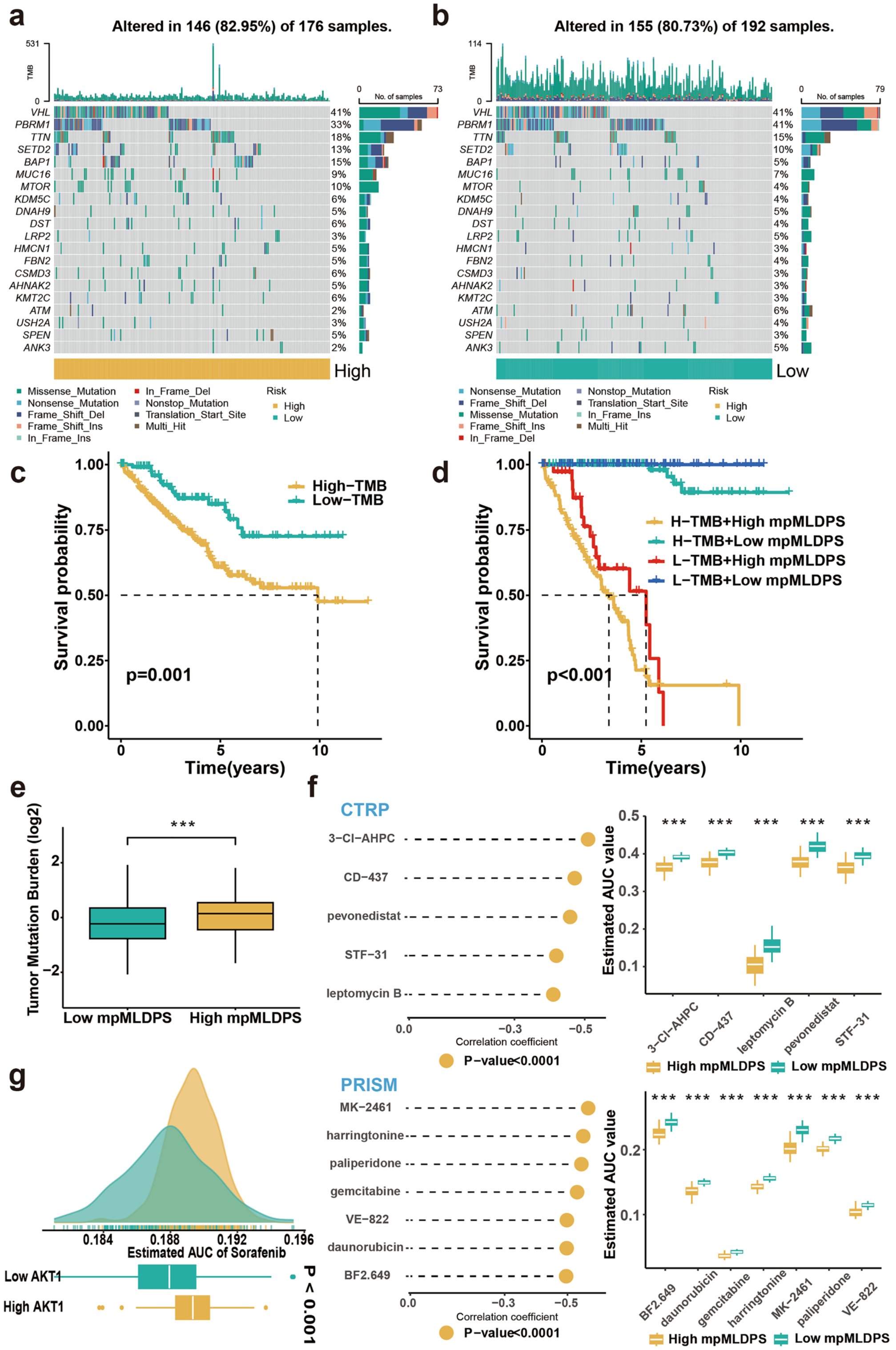

Fig. 5 Mutation landscape and drug discovery. **a** Landscape of the first 20 high-frequency mutated genes in the high mpMLDPS group. **b** Landscape of the first 20 high-frequency mutated genes in the low mpMLDPS group. **c** Kaplan–Meier survival curves of the OS between the high and low TMB groups. **d** K-M survival curves of the TMB subgroups and the mpMLDPS subgroups in a combined analysis. **e** TMB mutation burden between the two groups. **f** Drugs that responded to cell lines in the high mpMLDPS group from CTRP and PRISM. **g** Verification of the sensitivity of reduced AKT1 levels to sorafenib using CCLE, PRISM and CTRP. ***$p < 0.001$

within the mpMLDPS model, we analysed the expression differences of these eight genes between tumour and normal tissues. The results showed that PIF1, TIMP1, PLK1, E2F2, and BCL2A1 were highly expressed in tumour tissues, whereas CHDH, AGXT2, and AUH were expressed at lower levels in tumours (Supplementary Fig. S3a–h). Using the median expression levels of these genes, Kaplan–Meier survival analysis was performed for each gene's high- and low-expression subgroups (Supplementary Fig. S3i–p). The analysis revealed that high expression of PIF1, TIMP1, PLK1, E2F2, and BCL2A1 was associated with worse survival, while low expression of CHDH, AGXT2, and AUH predicted poorer survival outcomes. Among these, PIF1 drew particular attention, as it was not only highly expressed in tumours but also associated with significantly poorer prognosis in the high-expression group. PIF1 exhibited the highest HR among the eight model genes (Supplementary Fig. S3i). To further explore the functional implications of PIF1, over-representation analysis (ORA) was conducted. Gene Ontology (GO) enrichment analysis revealed that PIF1 was positively correlated with biological processes such as cell cycle regulation, chromosome function, DNA repair, and energy metabolism (Supplementary Fig. S4a). Similarly, KEGG pathway enrichment indicated that PIF1 played a significant role in processes like cellular growth and death, translocation and catabolism, replication and repair, and metabolism (Supplementary Fig. S4b). These findings establish PIF1 as a pivotal crosstalk gene linking PCD and MF, further highlighting its critical role in the mpMLDPS model.

Clinical relevance and expression of PIF1 in human ccRCC tissues

To investigate the clinical significance of PIF1 and its association with tumour progression, we analysed its expression across different clinicopathological parameters. As shown in Fig. 6a–e, PIF1 expression increased with advancing clinical stage, TNM grade, and tissue grade. These findings suggest that PIF1 may contribute to metastasis or be associated with greater tumour aggressiveness in RCC. To validate these observations, we performed IHC and WB on kidney cancer tissues and adjacent normal tissues. Both IHC and WB results confirmed that PIF1 expression was significantly higher in tumour tissues compared to adjacent normal tissues (Fig. 6f–h). Further validation using WB in normal renal epithelial cell lines and renal cancer cell lines demonstrated elevated PIF1 expression in renal cancer cell lines. Quantitative analysis indicated that the highest PIF1 expression levels were observed in the Caki-1 and 786-O cell lines (Fig. 6i). Based on these findings, these two cell lines were selected for subsequent experiments.

Effects of PIF1 silencing on the biological functions of renal cancer cell lines

To explore the role of PIF1 in the biological functions of renal cancer cells, we constructed a PIF1-silenced cell model using PIF1-shRNA lentivirus. WB analysis confirmed that the lentivirus effectively knocked down PIF1 expression in Caki-1 and 786-O cell lines (Fig. 7a). Functional assays were then conducted to evaluate the effects of PIF1 silencing. CCK-8 proliferation assays revealed that the knockdown of PIF1 significantly reduced the proliferation of Caki-1 and 786-O cells (Fig. 7b). Similarly, colony formation assays demonstrated marked inhibition of cell proliferation following PIF1 silencing (Fig. 7c). Furthermore, scratch assays and Transwell assays indicated that the migratory ability of renal cancer cells was significantly diminished after PIF1 knockdown (Fig. 7d, e). These results collectively highlight the critical role of PIF1 in promoting the proliferation and migration of renal cancer cells.

Impact of PIF1 on the cell cycle and mitochondrial function in renal cancer cells

To investigate the effect of PIF1 knockdown on mitochondrial function, we performed ROS and mitochondrial membrane potential assays. The results showed that silencing PIF1 significantly reduced the mitochondrial membrane potential (Fig. 8a) and increased intracellular ROS levels (Fig. 8b). Since the cell cycle is crucial for cell proliferation and growth, we also analysed its progression using flow cytometry. PIF1 knockdown led to cell cycle arrest in the G0/G1 phase, accompanied by a decreased proportion of cells in the S phase (Fig. 8c). To further elucidate the underlying mechanisms, we conducted Western blot (WB) analysis to assess mitochondrial function and cell cycle-related proteins after PIF1 knockdown (Fig. 8d). The results revealed significant changes in these indicators compared to the control group. Specifically: SOD2, a marker of mitochondrial antioxidant capacity, was significantly downregulated. CDK2 and CDK4, key regulators of cell cycle progression, exhibited reduced expression. In contrast, p21, a negative regulator of the cell cycle, and Cleaved Caspase-9, a marker of mitochondrial apoptosis, were significantly upregulated. These findings suggest that PIF1 knockdown disrupts mitochondrial function and induces cell cycle alterations, potentially contributing to impaired cell proliferation and increased apoptotic activity in renal cancer cells.

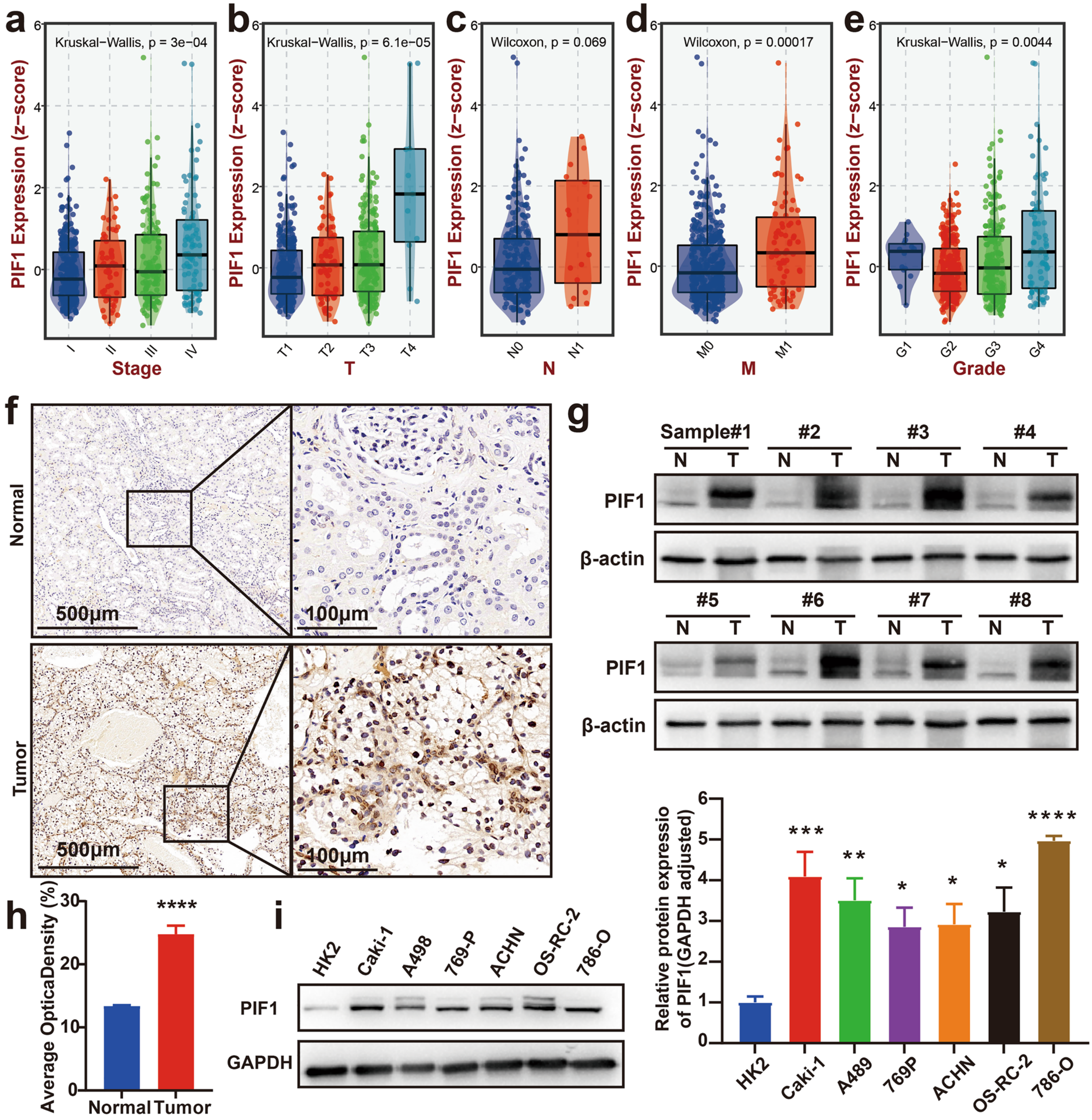

Fig. 6 Clinical relevance and expression of PIF1 in human ccRCC tissues. **a** Box plots of PIF1 gene expression differences in TCGA-KIRC cohort at different clinical stages. **b**–**d** Box plots of PIF1 gene expression differences in TCGA-KIRC cohort at different TNM stages. **e** Box plots of PIF1 gene expression differences in TCGA-KIRC cohort at different tissue grades. **f**–**h** Differential expression of PIF1 protein in ccRCC tissues and paracancerous tissues by IHC and WB. **i** WB detection of PIF1 protein levels in normal renal epithelial cell lines and renal cancer cell lines. *$p < 0.05$; **$p < 0.01$; ***$p < 0.001$; ****$p < 0.0001$

Discussion

PCD is a critical mechanism for maintaining immune system homeostasis [18], while its evasion is a hallmark of cancer progression [19]. Tumour cells employ diverse strategies to circumvent cell death mechanisms, thereby promoting proliferation, metastasis, and resistance to therapies [20, 21]. MF is tightly linked with PCD, with mounting evidence highlighting their joint roles in tumour growth, metastasis, and therapy resistance [22–24].

This study underscores the interplay between mitochondrial dysfunction and PCD in ccRCC. Among the 17 genes

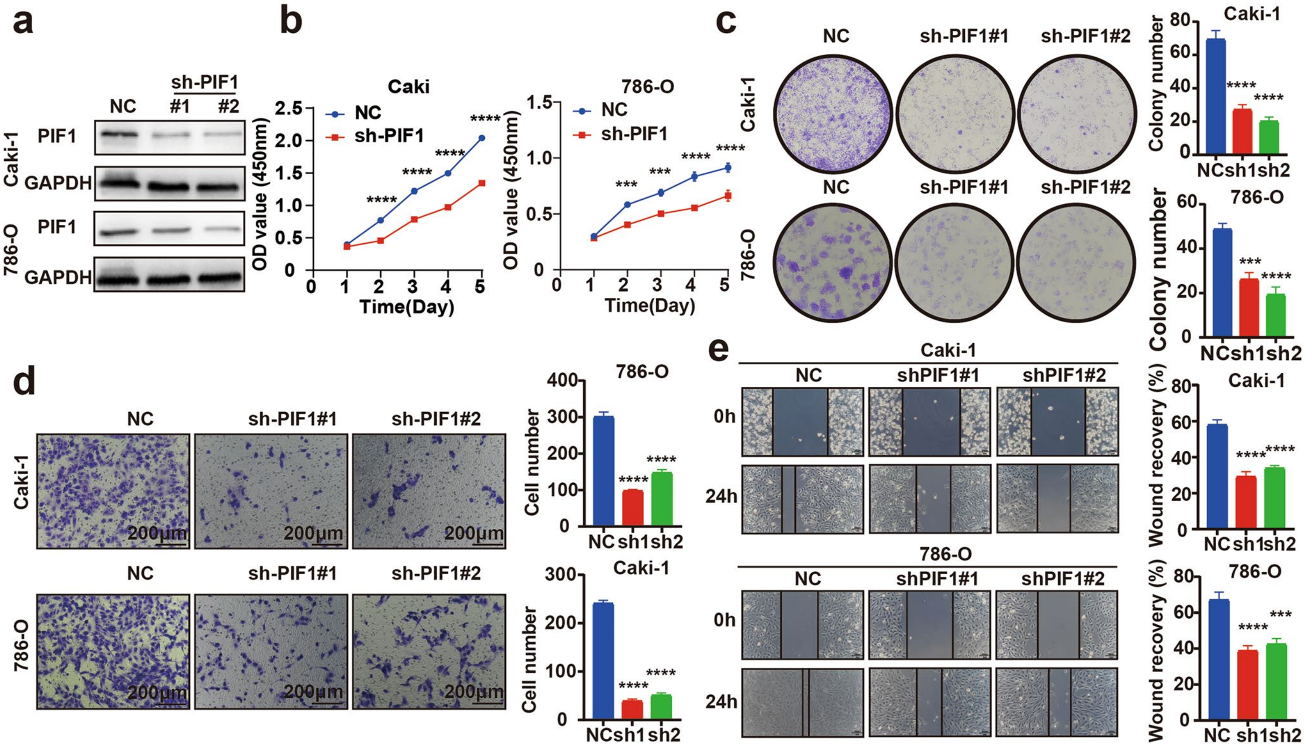

Fig. 7 Effect of silencing PIF1 on the biological function of RCC lines. **a** WB verified the effect of lentiviral silencing of PIF1. **b** CCK-8 assay to assess the effect of silencing PIF1 on RCC cell proliferation. **c** Clone formation assay to assess the effect of silencing PIF1 on the clone formation ability of RCC cells. **d** Transwell assay to assess the effect of silencing PIF1 on the migration ability of RCC cells. **e** Wound healing assay to assess the effect of silencing PIF1 on the migration ability of RCC cells. *$p < 0.05$; **$p < 0.01$; ***$p < 0.001$; ****$p < 0.0001$

identified, BIRC5 and BCL2A1 are key players in anti-apoptotic processes [25, 26], potentially supporting tumour cell survival by enhancing mitochondrial stability. EZH2, E2F2, and CDKN3 are involved in cell cycle regulation [27, 28], suggesting that their impact on the cell cycle may influence mitochondrial function and tumour proliferation. Further investigation of these genes could shed light on the roles of MF and PCD in ccRCC progression.

Patient heterogeneity often leads to varied responses to ccRCC immunotherapy. Mitochondrial dysfunction is closely associated with immune evasion, a key determinant of ICI efficacy. We observed that patients in the high mpMLDPS group exhibited a more immunosuppressive tumour microenvironment and reduced responsiveness to immunotherapy, suggesting that targeting MF and PCD pathways may improve therapeutic outcomes. Mitochondrial dysfunction can impair oxidative phosphorylation, leading to T-cell exhaustion through metabolic and epigenetic reprogramming [29, 30]. Furthermore, mitochondrial complex III disruption compromises Tregs by impairing immune regulatory gene expression [31], while mitochondrial integrity and metabolic reprogramming influence Treg differentiation and function [32, 33]. Additionally, myeloid-derived suppressor cells (MDSCs) exacerbate immune suppression through metabolic pathways impacted by mitochondrial dysfunction [34]. These findings underscore the significant role of mitochondrial dysfunction in reshaping the immune microenvironment.

RCC, as a metabolic disease, exhibits substantial energy metabolism reprogramming essential for rapid growth and survival [35–37]. Our study demonstrated that PIF1 knockdown leads to mitochondrial dysfunction, characterised by reduced mitochondrial membrane potential and elevated ROS levels, exacerbating oxidative stress. These findings align with the established role of mitochondrial dysfunction in promoting tumour cell death through ROS generation [38]. High ROS levels damage cellular lipids, proteins, and DNA, and drug resistance [39]. Previous studies have shown that PIF1 maintains cell cycle progression, protects against DNA damage, and prevents apoptosis under replication stress [13, 40]. Other reports revealed that PIF1 knockdown inhibits autophagy and induces apoptosis in pulmonary artery endothelial cells [41]. These observations suggest that PIF1 may influence mitochondrial function and ROS production indirectly via pathways involving antioxidant enzymes (e.g. SOD2, GPX), cell cycle regulation, DNA damage response, or autophagy. Further research is needed to elucidate the

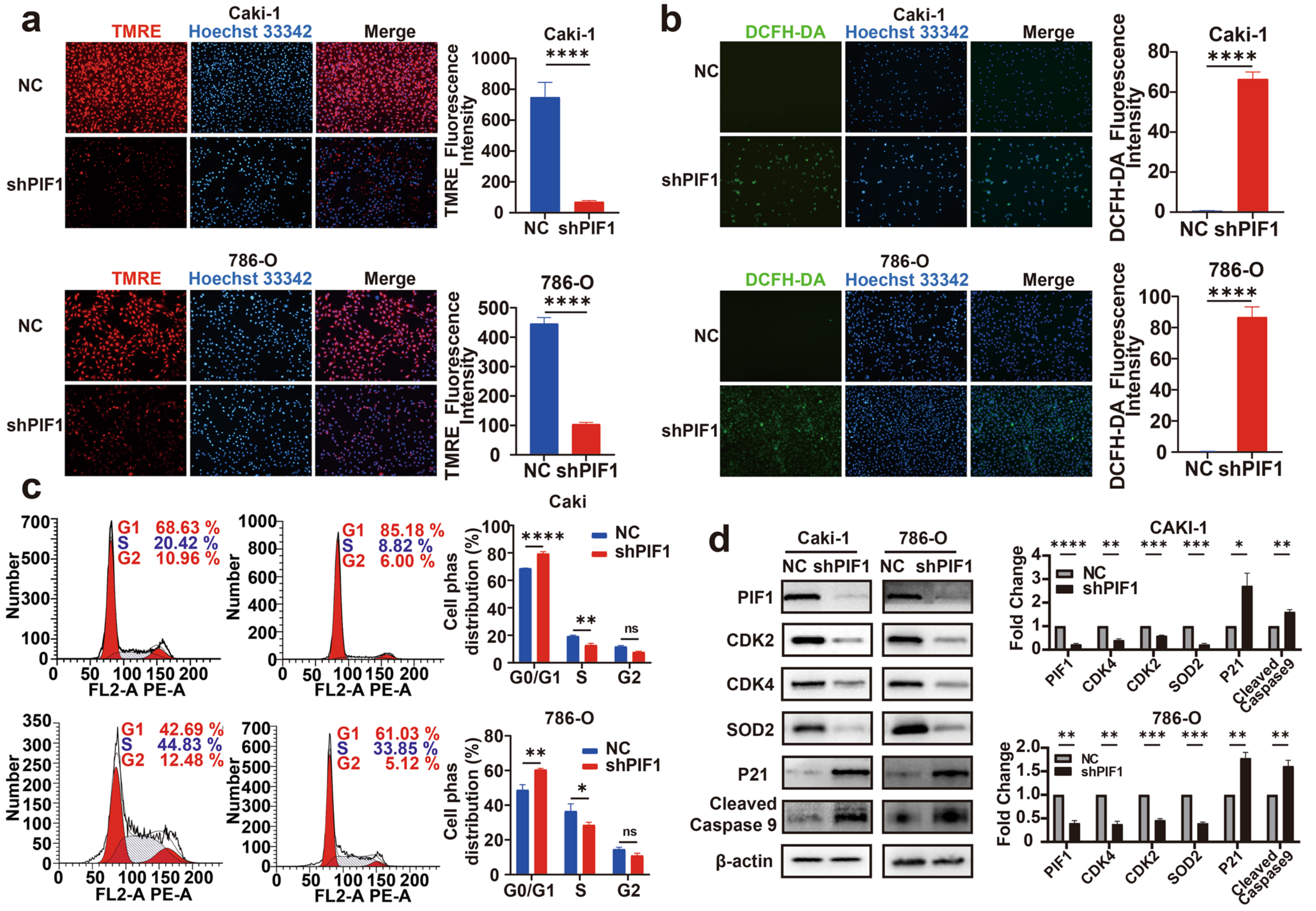

Fig. 8 PIF1 affects renal cancer cell cycle and mitochondrial function. **a** TMRE detection of mitochondrial membrane potential in Caki-1 and 786-O cells. **b** DCFH-DA detects cellular ROS levels. **c** Flow cytometry detection of the cell cycle. **d** WB detection of mitochondrial function and cell cycle-related indicators. *$p < 0.05$; **$p < 0.01$; ***$p < 0.001$; ****$p < 0.0001$

precise molecular mechanisms of PIF1 in ROS production and mitochondrial function, particularly in ccRCC.

Our cell cycle analysis revealed that PIF1 knockdown induces G0/G1 phase arrest and reduces the S-phase cell proportion, indicating its dual role in maintaining mitochondrial homeostasis and modulating cell cycle checkpoints to promote RCC cell growth and migration. These findings corroborate earlier research on PIF1 regulating apoptosis and pyroptosis in various cancers, including cervical, colon, and lung adenocarcinomas [13, 42, 43]. Although this study focuses on ccRCC, PIF1's potential in other cancers warrants exploration. Mitochondrial dysfunction and ROS generation similarly affect tumour progression in lung and breast cancers [44, 45], suggesting a broader role for PIF1 in tumour immune microenvironments and therapy responses across cancer types.

By integrating a set of genes related to PCD and MF, we developed a robust model that not only predicts patient survival but also provides insight into their likely response to immunotherapy. However, our study has some limitations. Firstly, this study was mainly based on bioinformatics analysis of a web-based database, and although some of the functions were experimentally validated, the stability and generalisation of the model need to be further verified. Secondly, although PIF1 shows promise as a targeted therapy, our study is far from reaching the stage of clinical application, and future experimental studies need to verify its clinical value.

Conclusions

In conclusion, mpMLDPS was significantly associated with PCD and MF and demonstrated superiority in prognostic prediction. The findings provide strong support for personalised risk assessment and immunotherapeutic interventions for ccRCC patients. Additionally, the high-impact genes included in the mpMLDPS signature offer novel perspectives for future studies on the role of PCD in MF.

Meanwhile, our study suggested that PIF1 is expected to be a novel target for the clinical treatment of ccRCC.

Supplementary Information The online version contains supplementary material available at https://doi.org/10.1007/s00262-025-03967-8.

Acknowledgements Not applicable

Authors' contributions Guang-Yang Cheng contributed to conceptualisation, writing—original draft, writing—review & editing, formal analysis, visualisation. Zhao-kai Zhou and Shi-qi Li helped in writing—original draft, writing—review & editing, formal analysis. Fu Peng and Shuai Yang helped in writing—review & editing, validation, software. Chuan-chuan Ren helped in writing—review & editing, funding acquisition, supervision. All authors reviewed the manuscript.

Funding This work was supported by the National Natural Science Foundation of China (Grant numbers [82000724]).

Data and materials availability Public data used in this work can be acquired from the TCGA Research Network portal (https://portal.gdc.cancer.gov/), Gene Expression Omnibus (http://www.ncbi.nlm.nih.gov/geo/) and ArrayExpress database (https://www.ebi.ac.uk/arrayexpress/).

Declarations

Conflict of interest The authors declare no competing interests.

Consent to participate Not applicable.

Consent for publication Not applicable.

Ethical approval consent to participate All ethical aspects of this study were approved by the Ethics Committee of the First Affiliated Hospital of Zhengzhou University (2024-KY-0999–001).

References

1. Zhu L, Wang J, Kong W, Huang J, Dong B, Huang Y et al (2019) LSD1 inhibition suppresses the growth of clear cell renal cell carcinoma via upregulating P21 signaling. Acta Pharm Sin B 9(2):324–334. https://doi.org/10.1016/j.apsb.2018.10.006
2. Xu J, Chang WH, Fong LWR, Weiss RH, Yu SL, Chen CH (2019) Targeting the insulin-like growth factor-1 receptor in MTAP-deficient renal cell carcinoma. Signal Transduct Target Ther 4:2. https://doi.org/10.1038/s41392-019-0035-z
3. Li W, Ye K, Li X, Liu X, Peng M, Chen F et al (2022) YTHDC1 is downregulated by the YY1/HDAC2 complex and controls the sensitivity of ccRCC to sunitinib by targeting the ANXA1-MAPK pathway. J Exp Clin Cancer Res 41(1):250. https://doi.org/10.1186/s13046-022-02460-9
4. Liang Z, Nong F, Zhao J, Wei D, Tang Q, Song J et al (2022) Heterogeneity in NK cell subpopulations may be involved in kidney cancer metastasis. J Immunol Res 2022:6378567. https://doi.org/10.1155/2022/6378567
5. Jenkins VK, Timmons AK, McCall K (2013) Diversity of cell death pathways: insight from the fly ovary. Trends Cell Biol 23(11):567–574. https://doi.org/10.1016/j.tcb.2013.07.005
6. Behl T, Makkar R, Anwer MK, Hassani R, Khuwaja G, Khalid A et al (2023) Mitochondrial dysfunction: a cellular and molecular hub in pathology of metabolic diseases and infection. J Clin Med 12(8):2882. https://doi.org/10.3390/jcm12082882
7. Nguyen TT, Wei S, Nguyen TH, Jo Y, Zhang Y, Park W et al (2023) Mitochondria-associated programmed cell death as a therapeutic target for age-related disease. Exp Mol Med 55(8):1595–1619. https://doi.org/10.1038/s12276-023-01046-5
8. Zhang H, Liu H, Shen Z, Lin C, Wang X, Qin J et al (2018) Tumor-infiltrating neutrophils is prognostic and predictive for postoperative adjuvant chemotherapy benefit in patients with gastric cancer. Ann Surg 267(2):311–318. https://doi.org/10.1097/SLA.0000000000002058
9. Cadiz F, Gormaz JG, Burotto M (2018) Breast cancer staging: is tnm ready to evolve? J Glob Oncol 4:1–3. https://doi.org/10.1200/JGO.17.00004
10. Huang Q, Li F, Liu L, Xu R, Yang T, Ma X et al (2023) Construction of EMT related prognostic signature for kidney renal clear cell carcinoma, through integrating bulk and single-cell gene expression profiles. Front Pharmacol 14:1302142. https://doi.org/10.3389/fphar.2023.1302142
11. Pei D, Xu C, Wang D, Shi X, Zhang Y, Liu Y et al (2022) A novel prognostic signature associated with the tumor microenvironment in kidney renal clear cell carcinoma. Front Oncol 12:912155. https://doi.org/10.3389/fonc.2022.912155
12. Yuan Y, Wang R, Luo M, Zhang Y, Guo F, Bai G et al (2022) A machine learning approach using XGBoost predicts lung metastasis in patients with ovarian cancer. Biomed Res Int 2022:8501819. https://doi.org/10.1155/2022/8501819
13. Gagou ME, Ganesh A, Thompson R, Phear G, Sanders C, Meuth M (2011) Suppression of apoptosis by PIF1 helicase in human tumor cells. Cancer Res 71(14):4998–5008. https://doi.org/10.1158/0008-5472.CAN-10-4404
14. Zhou Y, Cao Y, Liu W, Wang L, Kuang Y, Zhou Y et al (2023) Leveraging a gene signature associated with disulfidptosis identified by machine learning to forecast clinical outcomes, immunological heterogeneities, and potential therapeutic targets within lower-grade glioma. Front Immunol 14:1294459. https://doi.org/10.3389/fimmu.2023.1294459
15. Rath S, Sharma R, Gupta R, Ast T, Chan C, Durham TJ et al (2021) MitoCarta3.0: an updated mitochondrial proteome now with sub-organelle localization and pathway annotations. Nucleic Acids Res 49(1):1541–1547. https://doi.org/10.1093/nar/gkaa1011
16. Chen B, Khodadoust MS, Liu CL, Newman AM, Alizadeh AA (2018) Profiling tumor infiltrating immune cells with CIBERSORT. Methods Mol Biol 1711:243–259. https://doi.org/10.1007/978-1-4939-7493-1_12
17. Tei H, Miyake H, Fujisawa M (2015) Enhanced sensitivity to sorafenib by inhibition of Akt1 expression in human renal cell carcinoma ACHN cells both in vitro and in vivo. Hum Cell 28(3):114–121. https://doi.org/10.1007/s13577-015-0112-8

18. Blair PJ, Riley JL, Harlan DM, Abe R, Tadaki DK, Hoffmann SC et al (2000) CD40 ligand (CD154) triggers a short-term CD4(+) T cell activation response that results in secretion of immunomodulatory cytokines and apoptosis. J Exp Med 191(4):651–660. https://doi.org/10.1084/jem.191.4.651
19. Chen F, Zhong Z, Tan HY, Guo W, Zhang C, Cheng CS et al (2020) Suppression of lncRNA MALAT1 by betulinic acid inhibits hepatocellular carcinoma progression by targeting IAPs via miR-22-3p. Clin Transl Med 10(6):e190. https://doi.org/10.1002/ctm2.190
20. Ercolano G, De Cicco P, Ianaro A (2019) New drugs from the sea: pro-apoptotic activity of sponges and algae derived compounds. Mar Drugs 17(1):31. https://doi.org/10.3390/md17010031
21. Laubach V, Kaufmann R, Bernd A, Kippenberger S, Zoller N (2019) Extrinsic or intrinsic apoptosis by curcumin and light: still a mystery. Int J Mol Sci 20(4):905. https://doi.org/10.3390/ijms20040905
22. Abate M, Festa A, Falco M, Lombardi A, Luce A, Grimaldi A et al (2020) Mitochondria as playmakers of apoptosis, autophagy and senescence. Semin Cell Dev Biol 98:139–153. https://doi.org/10.1016/j.semcdb.2019.05.022
23. Tang M, Lin K, Ramachandran M, Li L, Zou H, Zheng H et al (2022) A mitochondria-targeting lipid-small molecule hybrid nanoparticle for imaging and therapy in an orthotopic glioma model. Acta Pharm Sin B 12(6):2672–2682. https://doi.org/10.1016/j.apsb.2022.04.005
24. Araiso Y, Tsutsumi A, Qiu J, Imai K, Shiota T, Song J et al (2019) Structure of the mitochondrial import gate reveals distinct preprotein paths. Nature 575(7782):395–401. https://doi.org/10.1038/s41586-019-1680-7
25. Nakamura Y, Suzuki S, Suzuki T, Ono K, Miura I, Satoh F et al (2006) MDM2: a novel mineralocorticoid-responsive gene involved in aldosterone-induced human vascular structural remodeling. Am J Pathol 169(2):362–371. https://doi.org/10.2353/ajpath.2006.051351
26. Brady SW, McQuerry JA, Qiao Y, Piccolo SR, Shrestha G, Jenkins DF et al (2017) Combating subclonal evolution of resistant cancer phenotypes. Nat Commun 8(1):1231. https://doi.org/10.1038/s41467-017-01174-3
27. Mikheev AM, Nabekura T, Kaddoumi A, Bammler TK, Govindarajan R, Hebert MF et al (2008) Profiling gene expression in human placentae of different gestational ages: an OPRU network and UW SCOR study. Reprod Sci 15(9):866–877. https://doi.org/10.1177/1933719108322425
28. Du K, Sun S, Jiang T, Liu T, Zuo X, Xia X et al (2022) E2F2 promotes lung adenocarcinoma progression through B-Myb- and FOXM1-facilitated core transcription regulatory circuitry. Int J Biol Sci 18(10):4151–70. https://doi.org/10.7150/ijbs.72386
29. Yu YR, Imrichova H, Wang H, Chao T, Xiao Z, Gao M et al (2020) Disturbed mitochondrial dynamics in CD8(+) TILs reinforce T cell exhaustion. Nat Immunol 21(12):1540–1551. https://doi.org/10.1038/s41590-020-0793-3
30. Liu M, Fu X, Yi Q, Xu E, Dong L (2024) Impaired mitochondrial oxidative phosphorylation induces CD8(+) T cell exhaustion. Biochem Biophys Res Commun 734:150738. https://doi.org/10.1016/j.bbrc.2024.150738
31. Weinberg SE, Singer BD, Steinert EM, Martinez CA, Mehta MM, Martinez-Reyes I et al (2019) Mitochondrial complex III is essential for suppressive function of regulatory T cells. Nature 565(7740):495–499. https://doi.org/10.1038/s41586-018-0846-z
32. Chen Y, Guo M, Xie K, Lei M, Chai Y, Zhang Z et al (2024) Progranulin promotes regulatory T cells plasticity by mitochondrial metabolism through AMPK/PGC-1alpha pathway in ARDS. Clin Immunol 261:109940. https://doi.org/10.1016/j.clim.2024.109940
33. Ozay EI, Sherman HL, Mello V, Trombley G, Lerman A, Tew GN et al (2018) Rotenone treatment reveals a role for electron transport complex I in the subcellular localization of key transcriptional regulators during T helper cell differentiation. Front Immunol 9:1284. https://doi.org/10.3389/fimmu.2018.01284
34. Wu H, Zhao X, Hochrein SM, Eckstein M, Gubert GF, Knopper K et al (2023) Mitochondrial dysfunction promotes the transition of precursor to terminally exhausted T cells through HIF-1alpha-mediated glycolytic reprogramming. Nat Commun 14(1):6858. https://doi.org/10.1038/s41467-023-42634-3
35. Abu Aboud O, Donohoe D, Bultman S, Fitch M, Riiff T, Hellerstein M et al (2015) PPARalpha inhibition modulates multiple reprogrammed metabolic pathways in kidney cancer and attenuates tumor growth. Am J Physiol Cell Physiol 308(11):C890–C898. https://doi.org/10.1152/ajpcell.00322.2014
36. Chakraborty S, Balan M, Sabarwal A, Choueiri TK, Pal S (2021) Metabolic reprogramming in renal cancer: events of a metabolic disease. Biochim Biophys Acta Rev Cancer 1876(1):188559. https://doi.org/10.1016/j.bbcan.2021.188559
37. Boguslawska J, Poplawski P, Alseekh S, Koblowska M, Iwanicka-Nowicka R, Rybicka B et al (2019) MicroRNA-mediated metabolic reprograming in renal cancer. Cancers (Basel) 11(12):1825. https://doi.org/10.3390/cancers11121825
38. Wang Y, Zhang L, Zhao G, Zhang Y, Zhan F, Chen Z et al (2022) Homologous targeting nanoparticles for enhanced PDT against osteosarcoma HOS cells and the related molecular mechanisms. J Nanobiotechnology 20(1):83. https://doi.org/10.1186/s12951-021-01201-y
39. Ribeiro LC, Rodrigues L, Quincozes-Santos A, Tramontina AC, Bambini-Junior V, Zanotto C et al (2012) Caloric restriction improves basal redox parameters in hippocampus and cerebral cortex of Wistar rats. Brain Res 1472:11–19. https://doi.org/10.1016/j.brainres.2012.07.021
40. Chen B, Hua Z, Gong B, Tan X, Zhang S, Li Q et al (2020) Downregulation of PIF1, a potential new target of MYCN, induces apoptosis and inhibits cell migration in neuroblastoma cells. Life Sci 256:117820. https://doi.org/10.1016/j.lfs.2020.117820
41. Zhao Y, Wu J, Guan S, Xue T, Wei X, Cao D et al (2023) PIF1 promotes autophagy to inhibit chronic hypoxia induced apoptosis of pulmonary artery endothelial cells. Int J Chron Obstruct Pulmon Dis 18:1319–1332. https://doi.org/10.2147/COPD.S406453
42. Zhang T, Wu DM, Luo PW, Liu T, Han R, Deng SH et al (2022) CircNEIL3 mediates pyroptosis to influence lung adenocarcinoma radiotherapy by upregulating PIF1 through miR-1184 inhibition. Cell Death Dis 13(2):167. https://doi.org/10.1038/s41419-022-04561-x
43. Wang J, Zhu X, Ying P, Zhu Y (2020) PIF1 affects the proliferation and apoptosis of cervical cancer cells by influencing TERT. Cancer Manag Res 12:7827–7835. https://doi.org/10.2147/CMAR.S265336
44. Zhang J, Pan L, Zhang Q, Zhao Y, Wang W, Lin N et al (2023) MFN2 deficiency affects calcium homeostasis in lung adenocarcinoma cells via downregulation of UCP4. FEBS Open Bio 13(6):1107–1124. https://doi.org/10.1002/2211-5463.13591
45. Shen L, Fang H, Chen T, He J, Zhang M, Wei X et al (2010) Evaluating mitochondrial DNA in cancer occurrence and development. Ann N Y Acad Sci 1201:26–33. https://doi.org/10.1111/j.1749-6632.2010.05635.x